

Dynamical Properties of Molecular Cloud Complexes in Galaxies at the Epoch of Reionization

T. K. Daisy Leung^{1,2}, Andrea Pallottini^{3,4}, Andrea Ferrara^{4,5}, and Mordecai-Mark Mac Low^{2,6}

¹ Department of Astronomy, Space Sciences Building, Cornell University, Ithaca, NY 14853, USA; tleung@astro.cornell.edu

² Center for Computational Astrophysics, Flatiron Institute, 162 Fifth Avenue, New York, NY 10010, USA

³ Centro Fermi, Museo Storico della Fisica e Centro Studi e Ricerche “Enrico Fermi”, Piazza del Viminale 1, Roma, 00184, Italy

⁴ Scuola Normale Superiore, Piazza dei Cavalieri 7, I-56126 Pisa, Italy

⁵ Kavli Institute for the Physics and Mathematics of the Universe (WPI), University of Tokyo, Kashiwa 277-8583, Japan

⁶ American Museum of Natural History, 79th St. at Central Park West, New York, NY 10024, USA

To be Submitted.

Abstract

We study the properties of molecular cloud complexes (MCCs) using cosmological zoom-in simulation of a $z \simeq 6$ prototypical galaxy (“Althæa”). We identify MCCs using an H₂ density-based clump finder, and compare their mass, size, velocity dispersion, gas surface density, and virial parameter to observations. In Althæa, MCC masses are in the range of $10^{5.5-8.5} M_{\odot}$, with sizes $R \lesssim 200$ pc. We identify gravitationally unstable MCCs both via Toomre Q_{eff} analysis and the more observationally accessible virial parameter (α_{vir}) analysis. MCCs in the main disk of Althæa are globally stable, but their internal substructures have low α_{vir} and Q_{eff} values, indicative of instability to collapse. Their velocity dispersion and gas surface density are systematically higher than those observed in nearby galaxies, but comparable to starburst galaxies. We show that large-scale rotation is an important contributor to the velocity dispersion of some MCCs, even in the highly disturbed phase of Althæa. High resolution imaging of the first galaxies with the Atacama Large (sub-)Millimeter Array (ALMA) and the Next Generation Very Large Array (ngVLA) on $\lesssim 40$ pc are necessary to shed light on the star-forming gas dynamics since the cosmic dark ages.

Keywords: methods: data analysis – galaxies: high-redshift – galaxies: ISM – galaxies: evolution – galaxies: formation – galaxies: starburst – stars: formation

1. Introduction

The growth of galaxies and their subsequent evolution are governed by the baryon cycle—galaxies accrete gas from the intergalactic medium (IGM) either directly from the cosmic web, or through mergers with other galaxies. This gas fuels star formation and feeds central supermassive black holes. Subsequent feedback replenishes and enriches the circumgalactic medium by expelling some part of this material. Early galaxies are more gas-rich and their molecular fraction possibly higher than present-day galaxies.

Such massive gas inflows trigger gravitational instabilities that lead to the formation of molecular cloud complexes (MCCs) that are typically more massive ($M_{\text{gas}} \simeq 10^9 M_{\odot}$) and extended (\simeq sub-kpc) than those observed in nearby galaxies (e.g., Gabor & Bournaud 2013; Hopkins et al. 2014; Inoue et al. 2016). Some theoretical works argue that the migration of such giant massive clumps are largely responsible for the buildup of the bulges of massive galaxies at redshift $z \sim 0$ (e.g., Ceverino et al. 2010).

Early galaxies have higher star formation rates (SFR; Behroozi et al. 2013; Sparre et al. 2015; Maiolino et al. 2015; Dunlop et al. 2017) and smaller sizes (e.g., Bouwens et al. 2011; Ono et al. 2013) compared to the local population. As a consequence, we expect them to be significantly more ionized, and have intense and hard interstellar radiation fields (ISRF). Since their metallicity and dust content are also expected to be lower in these early evolutionary stages, shield-

ing of UV photons—responsible for the photoheating of the gas—is strongly reduced. Such differences in turn affect the regulation of the thermal and chemical state of the multi-phase interstellar medium (ISM). Studying ISM properties of early galaxies is essential for understanding how star formation proceeds under more extreme conditions. Even in the local Universe, where detailed observations can be made, variations in molecular cloud properties have been observed between different galaxy populations (see e.g., Hughes et al. 2010, 2013). Given that high- z galaxies statistically represent the early evolutionary stages of present-day galaxies, it is thus reasonable to pose the question: *what are the physical properties of molecular cloud structures in early galaxies, and how do they differ from those found in local galaxy populations?*

FIR fine-structure lines (e.g., [CII], [NII], and [OIII]), and CO and [CI] lines are key diagnostics for constraining the ISM conditions of galaxies. They also provide highly complementary information on different ISM phases (ionized, atomic, molecular; e.g., Scoville & Solomon 1974; Rubin 1985; Malhotra et al. 2001). Global measurements of these diagnostics in high- z galaxies have provided preliminary information on their global properties (e.g., gas masses, gas temperature, and radiation field intensity). However, spatially resolving their ISM is necessary to fully understand many aspects of galaxy evolution and the physics behind their intense star formation ($\text{SFR} \sim 100-3000 M_{\odot} \text{ yr}^{-1}$). To date, spatially resolved ISM properties of high- z galaxies have only been mapped in a handful of (strongly-lensed) galaxies at

intermediate- z , using tracers such as dust continuum, CO, and [CII] lines (e.g., Swinbank et al. 2011; Hodge et al. 2015; Ferkinhoff et al. 2015; Hodge et al. 2016; Leung et al. 2019). These studies find that galaxies close to the peak of cosmic star formation ($z \sim 2$), are more molecular gas-rich, turbulent, and clumpy than nearby galaxies.

Earlier epochs still represent an essentially uncharted territory for ISM investigations. At present, it remains unclear how star formation proceeds in the (sub-) L^* galaxy population at $z \gtrsim 6$ which is responsible for producing the bulk of the UV photons that reionized the Universe. While ALMA has enabled the detection of [CII] 158 μm and CO line emission in normal ($\text{SFR} < 100 M_\odot \text{ yr}^{-1}$) galaxies at $z > 6$ over the past few years (e.g., Carniani et al. 2018; D’Odorico et al. 2018), the first spatially resolved observations are just starting to become available (Jones et al. 2017; Smit et al. 2018).

To understand the physical properties of MCCs in early galaxies, we have undertaken a detailed numerical study whose aim is to characterize the dynamical properties of the star-forming MCCs in prototypical (i.e., L^*) galaxies in the Epoch of Reionization (EoR).

The paper is structured as follows⁶. We start by providing some physical background in §2. In §3, we describe the setup of our simulation and properties of our main galaxy (Althæa). In §4, we describe the method used to identify MCCs, and present the formalism within which we interpret the results. In §5, we present the results and the scaling relations for the MCCs. We then interpret the results and discuss the implications of our findings in §6, and give our conclusions in §7.

2. Physical Background

We begin by introducing some basic material concerning notable physical ("Larson") relations characterizing MCCs, and the gravitational instability of galactic disks, which might be driving MCC formation. Such notions will be used in the subsequent analysis of our simulations.

2.1. Larson relations and virial parameter

Larson (1981) discussed a number of relations among Galactic molecular cloud properties, namely the linewidth-size, density-size, and mass-size relations. Larson relations are routinely used for comparing properties of molecular structures in different galactic environments. They also represent a useful framework to analyze our results as they have been argued to arise from the interplay between gravity and turbulence encoded in the virial theorem (however, note the alternative interpretation involving gravitational collapse by Ballesteros-Paredes et al. 2011a).

The virial theorem for a distribution of unmagnetized gas

⁶ Throughout this paper, we adopt a concordance cosmology, with total matter, vacuum and baryonic densities in units of the critical density $\Omega_\Lambda = 0.692$, $\Omega_m = 0.308$, $\Omega_b = 0.0481$, Hubble constant $H_0 = 100 h \text{ km s}^{-1} \text{ Mpc}^{-1}$ with $h = 0.678$, spectral index $n = 0.967$ and $\sigma_8 = 0.826$ (Planck Collaboration et al. 2014).

can be written as (McKee & Zweibel 1992)

$$\frac{1}{2}\ddot{\mathcal{I}} = 2(\mathcal{T} - \mathcal{T}_{\text{ext}}) + \mathcal{W}, \quad (1)$$

where $\ddot{\mathcal{I}}$ is the second time derivative of the Lagrangian moment of inertia, \mathcal{T} is the internal energy of the gas, \mathcal{T}_{ext} is external pressure support, and \mathcal{W} is the gravitational energy. Let us specialize to the case of a spherical self-gravitating molecular cloud of mass M_{gas} , radius R , and root-mean-square velocity dispersion σ , accounting for both thermal and turbulent contributions. Defining P_{ext} as the external pressure, Equation 1 can be written as

$$\frac{1}{2}\ddot{\mathcal{I}} = 3M\sigma^2 - 4\pi P_{\text{ext}}R^3 - \Gamma \frac{GM^2}{R}, \quad (2)$$

where Γ is a geometrical factor that is equal to 3/5 for a uniform sphere; in Equation 2 the terms on the right-hand side represent the kinetic energy, external pressure, and gravitational potential energy terms.

Motivated by Larson’s linewidth-size relation (Larson 1981) and the work by Heyer et al. (2009), we assume equilibrium (i.e., $\ddot{\mathcal{I}} = 0$), define the cloud surface density as $\Sigma = M/\pi R^2$, and rewrite the previous equation as

$$\frac{\sigma^2}{R} = \frac{1}{3} \left(\frac{4P_{\text{ext}}}{\Sigma} + \frac{3}{5}\pi G\Sigma \right), \quad (3)$$

which further reduces to

$$\frac{\sigma^2}{R} = \frac{\pi}{5}G\Sigma, \quad (4)$$

if the external pressure $P_{\text{ext}} = 0$. For this case (often referred to as simple virial equilibrium) from the balance between kinetic and gravity terms we can define the virial parameter as

$$\alpha_{\text{vir}} \equiv \frac{5\sigma^2 R}{GM_{\text{gas}}} = \frac{5\sigma_{\text{gas}}^2}{\pi G \Sigma R}, \quad (5)$$

Based on Equation 4, a one-to-one mapping between σ_{gas}^2/R and Σ is therefore expected for a virialized cloud, since $\sigma_{\text{gas}}^2/R \propto \Sigma$. Deviations from this relation are usually attributed to a significant contribution from external pressure as per Equation 3 (see e.g., Heyer et al. 2009; Hughes et al. 2010, 2013; Meidt et al. 2013).

Summarizing, the virial parameter can be used to quantify the stability/boundedness of a molecular cloud. Accounting for the external pressure, a virial parameter of $\alpha_{\text{vir}} \lesssim 2$ would be unstable (Bertoldi & McKee 1992). Such a criterion is often used in observations (see e.g., Kauffmann et al. 2017b).

In cases where stellar component plays an important role in the dynamics, the virial parameter becomes

$$\alpha_{\text{vir,tot}} \equiv \frac{5R}{G(M_{\text{gas}} + M_\star)} \frac{M_{\text{gas}}\sigma_{\text{gas}}^2 + M_\star\sigma_\star^2}{M_{\text{gas}} + M_\star}, \quad (6)$$

where M_\star is the stellar mass within the MCC volume. (DL: Should we leave out σ_\star since stellar motions shouldn’t affect the gas?)

2.2. Toomre stability analysis

The onset of gravitational instability is tightly connected to star formation (e.g., Kennicutt 1989; Wang & Silk 1994; Li et al. 2005, 2006). For axisymmetric modes, the dispersion relation for the growth of density perturbations in a rotating, turbulent disk of finite thickness h is described by

$$\omega^2 = \kappa^2 - \frac{2\pi G \Sigma |k|}{1 + |k|h} + \sigma_{\text{disk}}^2 k^2, \quad (7)$$

where k is the wavenumber and κ is the epicyclic frequency, defined as:

$$\kappa^2 \equiv \frac{2\Omega}{\varpi} \frac{d}{d\varpi} (\varpi^2 \Omega). \quad (8)$$

(Romeo 1992). In Equation 7 the terms on the right hand side are related to rotation, self-gravity and internal pressure, respectively. Heuristically, the instability can be understood by considering the scale at which gravitational potential overcomes the internal energy. Gravity dominates at scales $L > L_J$, where L_J is the Jeans length. However, differential rotation in disk galaxies can stabilize perturbations that might otherwise collapse for $L > L_{\text{rot}}$, where L_{rot} is set by κ . As a result, disks are unstable to gravitational collapse on scales between $L_J < L < L_{\text{rot}}$.

From the dispersion relation, a parameter Q can be derived such that $Q < 1$ when instability occurs, that reproduces this inequality to order unity. For a collisionless fluid—such as an ensemble of stars—this parameter is (Toomre 1964)

$$Q_* \equiv \frac{\sigma_* \kappa}{3.36 G \Sigma_*}. \quad (9)$$

The equivalent parameter for a collisional gas was derived by Goldreich & Lynden-Bell (1965)

$$Q_{\text{gas}} \equiv \frac{\sigma_{\text{gas}} \kappa}{\pi G \Sigma_{\text{gas}}}. \quad (10)$$

In the thin disk approximation ($kh \ll 1$), instability ($\omega^2 < 0$ in Equation 7) occurs on scales k such that $Q < Q_{\text{crit}} \simeq 1$ (or equivalently $\omega^2 < 0$). A frequently used observable proxy for Q is the ratio of disk circular velocity to root-mean-square velocity dispersion $v_{\text{circ}}/\sigma_{\text{disk}}$ (e.g., García-Burillo et al. 2003; Genzel et al. 2011; Kassin et al. 2012; Leung et al. 2019).

In our stability analysis, we account for the combined effect of gas and stars (derived exactly by Rafikov 2001), and for the non-negligible disk thickness. This is done by adopting an approximation for an effective two-component Q_{eff} parameter (i.e., Romeo & Wiegert 2011, see also Inoue et al. 2016). The effect of disk thickness modifies the Q parameter for gas and stars by accounting for the vertical velocity dispersion

$$T_x = \begin{cases} 0.8 + 0.7 \left(\frac{\sigma_z}{\sigma_r} \right) & \text{if } \sigma_z \lesssim 0.5 \times \sigma_r \\ 1 + 0.6 \left(\frac{\sigma_z}{\sigma_r} \right) & \text{if } \sigma_z \gtrsim 0.5 \times \sigma_r \end{cases} \quad (11)$$

and

$$Q_x^{\text{thick}} = T_x Q, \quad (12)$$

with x indicating either gas or stars. The combined effect of gas and stars can then be accounted for by writing

$$Q_{\text{eff}}^{-1} = \begin{cases} \frac{w}{Q_*^{\text{thick}}} + \frac{1}{Q_{\text{gas}}^{\text{thick}}} & \text{if } Q_*^{\text{thick}} \geq Q_{\text{gas}}^{\text{thick}} \\ \frac{1}{Q_*^{\text{thick}}} + \frac{w}{Q_{\text{gas}}^{\text{thick}}} & \text{if } Q_*^{\text{thick}} \leq Q_{\text{gas}}^{\text{thick}} \end{cases} \quad (13)$$

where the relative weight w is defined as

$$w \equiv \frac{2\sigma_* \sigma_{\text{gas}}}{\sigma_*^2 + \sigma_{\text{gas}}^2}, \quad (14)$$

Conceptually, the finite disk thickness reduces the gravity in the vertical direction, thereby making it easier for a system to maintain stability, and thus lowering the critical Toomre Q_{crit} from $\simeq 1$ to 0.67 (Goldreich & Lynden-Bell 1965). On the other hand, including the contribution of the stellar component promotes gravitational instability, and thus increases Q_{crit} , more-so if the stars have low velocity dispersion. As a rule of thumb, $Q_{\text{crit}} = 1.34$ for $Q_{\text{gas}} = Q_*$.

3. Numerical Simulations

The simulations used in this work are described by Pallottini et al. 2017a,b and are briefly summarized here. SERRA⁷ is a suite of cosmological zoom-in simulations performed using Eulerian hydrodynamics and adaptive mesh refinement (AMR) techniques to achieve high spatial resolution in regions of interest (e.g., regions of high density). In particular, it uses a modified version of RAMSES (Teyssier 2002) as the AMR backend. The simulation used here covers a comoving box of $20 \text{ Mpc } h^{-1}$ in size. The simulation zooms in on a target halo of mass $M_{\text{DM}} \simeq 10^{11} M_{\odot}$. The Lagrangian region of the halo ($2.1 \text{ Mpc } h^{-1}$) has a dark matter mass resolution of $\simeq 6 \times 10^4 M_{\odot}$, equivalent at initial density to a baryonic mass resolution of $1.2 \times 10^4 M_{\odot}$. This region is spatially refined with a quasi-Lagrangian criterion based on a mass threshold, so that a cell is refined if its total (dark+baryonic) mass exceeds the mass resolution by a factor of eight. The finest refined cell allowed in the zoom in region has size $l_{\text{cell}} \simeq 30 \text{ pc}$ (at $z = 6$), i.e. sizes are comparable to the sizes of local giant molecular clouds (e.g., Sanders et al. 1985; Federrath & Klessen 2013; Goodman et al. 2014). The models include a non-equilibrium chemical network following e^- , H^+ , H^- , He , He^+ , He^{++} , H_2 , and H_2^+ (Grassi et al. 2014; Bovino et al. 2016). Of particular importance here is that abundances are calculated using an on-the-fly non-equilibrium formation of molecular hydrogen scheme described by Pallottini et al. (2017a).

Star formation is modeled using an H_2 -based prescription of the Schmidt-Kennicutt relation (Krumholz et al. 2009). We adopt stellar tracks from STARBURST99 and include stellar feedback from supernovae (SNe) as well as winds from OB and asymptotic giant branch stars. Coupling to the gas is

⁷ Greenhouse in Italian.

implemented via a sub-grid model for blastwaves, which accounts for radiative energy losses inside the cell. The remaining energy is injected into the ISM in kinetic and thermal energy forms. Radiation pressure on dust and gas is also included. Photoionization from local sources is neglected in this simulation (see Pallottini et al., in prep. 2019; Decataldo et al., in prep. 2019, for its effect). Via feedback processes the gas can acquire energy both thermal and non-thermal form (Agertz et al. 2013); the latter is a term that mimics unresolved turbulence: such non-thermal energy is not affected by cooling but rather is dissipated on the eddy turn-over time scale (Mac Low 1999). See Pallottini et al. (2017b) for further details.

The simulation zooms in on a galaxy named after the flower Althæa whose properties are given in Pallottini et al. (2017a) and are briefly summarized in the following. Althæa is a Lyman-break galaxy that at $z \simeq 6$ is hosted by a dark matter halo of mass $M_{\text{DM}} \simeq 10^{11} M_{\odot}$ at the center of a cosmic web knot, and accretes mass from the IGM mainly via three filaments of length $\simeq 100$ kpc. Althæa has a stellar mass of $M_{\star} \simeq 3 \times 10^{10} M_{\odot}$, a metallicity of $Z \simeq 0.5 Z_{\odot}$, a molecular gas mass of $M_{\text{H}_2} \simeq 5 \times 10^7 M_{\odot}$, and a SFR of $30 - 80 M_{\odot} \text{ yr}^{-1}$. The specific SFR of Althæa is $\text{sSFR} \equiv \text{SFR}/M_{\star} \simeq 4 - 40 \text{ Gyr}^{-1}$, compatible with the sSFR vs. M_{\star} relation observed at high redshift (Jiang et al. 2016), which is higher than normal local galaxies. The effective stellar radius of Althæa is ~ 0.5 kpc and the dark matter virial radius is $r_{200} \simeq 15$ kpc.

3.1. Star Formation History

One of the main advantages of studying galaxies in simulations is that we can examine how their dynamical properties evolve with time, which is interesting in order to understand the physical processes that determine the morphology and dynamical properties of galaxies, which in turn affect their star formation. The star formation history⁸ of Althæa is shown in Figure 1. The SFR of Althæa varies between $\sim 30 - 80 M_{\odot} \text{ yr}^{-1}$ as it evolves from an actively accreting phase to a starburst phase after a merger, and then back to a relatively quiescent phase, over the simulated ≈ 700 Myr.

Given the stochastic nature of Althæa in its star formation history, we mostly focus on few of its most extreme evolutionary stages in this work (see §5.2). These phases correspond to (a) an intensely accreting phase and (b) a starburst phase (Figure 1). We are interested in determining whether MCC properties are sensitive to these different dynamical conditions. For completeness, we also show the scaling relations examined for the other evolutionary stages traced in the simulation (see §5.3).

In §6.2, we investigate the importance of rotation support from large-scale motions in the MCC dynamics by comparing

⁸ Note that here the SFR is calculated based on the stellar mass formed in the last 4 Myr within 3.5 kpc from the galaxy center of mass. The SFR plotted in Figure 2 of Pallottini et al. (2017b) is a factor of two higher since there the SFR accounts for the contribution from massive satellite galaxies within the virial radius (≈ 15 kpc).

their properties in the disturbed phase of Althæa and in the disk-like ordered phase.

Throughout this paper, we describe the dense gas regions outside the main disk of Althæa as satellite galaxies. The distinction between clumps and satellites is admittedly somewhat ambiguous, though, and we consider it only as a working one.

(AF: To be discussed at the end)

4. Molecular Cloud Complexes

4.1. Identification

To identify the molecular complexes, we use a customized version of the clump-finding algorithm available in the PYTHON package YT (Turk et al. 2011), which was initially described in Smith et al. (2009) and modified since. The latest version of the default YT clump finder decomposes the zones of the simulation into non-overlapping tiles, which are stored in a three-dimensional tree that can be processed using k -dimensional tree algorithms. It then identifies the contours of a variable field (here, the density field) within a tile and connects them across the tiles. In the customized version used for this study, we enhanced the stability of the code. Due to the nature of our AMR simulation, we regrid the simulation data into uniform grids. The grid size is defined based on the highest resolution of the simulation data, i.e., the less refined regions are supersampled in the resulting uniform grids.

In the clump-finding process (in position-position-position space; PPP), we employ a set of different density thresholds defined based on the molecular hydrogen density of Althæa at different evolutionary stages ($z = 6.0 - 7.2$). We note that this process is the three-dimensional analog to identifying molecular structures based on the noise levels in position-position-velocity (PPV) maps that observers obtain with telescopes, using molecular line tracers such as CO, CS, and HCN. This is commonly done by identifying clumps based on/after applying S/N-clipping, using tools such as AIPS’s task SERCH, CLUMPFIND, and CPROPS; Williams et al. 1994; Oka et al. 2001; Rosolowsky & Leroy 2006; Rosolowsky et al. 2008). Existing studies find a good correspondence in the dynamical properties extracted in PPV- versus PPP-space for well-isolated structures (Ballesteros-Paredes & Mac Low 2002a; Heitsch et al. 2009; Shetty et al. 2010; Beaumont et al. 2013; Pan et al. 2015, but see Ballesteros-Paredes & Mac Low 2002a and Shetty et al. 2010 for a discussion on caveats and limitations).

In Figure 2, we show the distribution of H_2 number density n_{H_2} for Althæa during its accreting phase, including the contribution from the gas within 3.5 kpc from the galaxy center. We note that the distribution is almost flat for $n_{\text{H}_2} \gtrsim 1 \text{ cm}^{-3}$ and it samples the range of densities where clumps are found based on morphological analysis⁹ (Pallottini et al. 2017b). In each evolutionary stage, we identify MCCs by

⁹ For $n_{\text{H}_2} \gtrsim 1 \text{ cm}^{-3}$, the fourth Minkowski functional of the H_2 density field is significantly larger than zero. This implies that the field is made of isolated components. See Fig. 6 in Pallottini et al. (2017b).

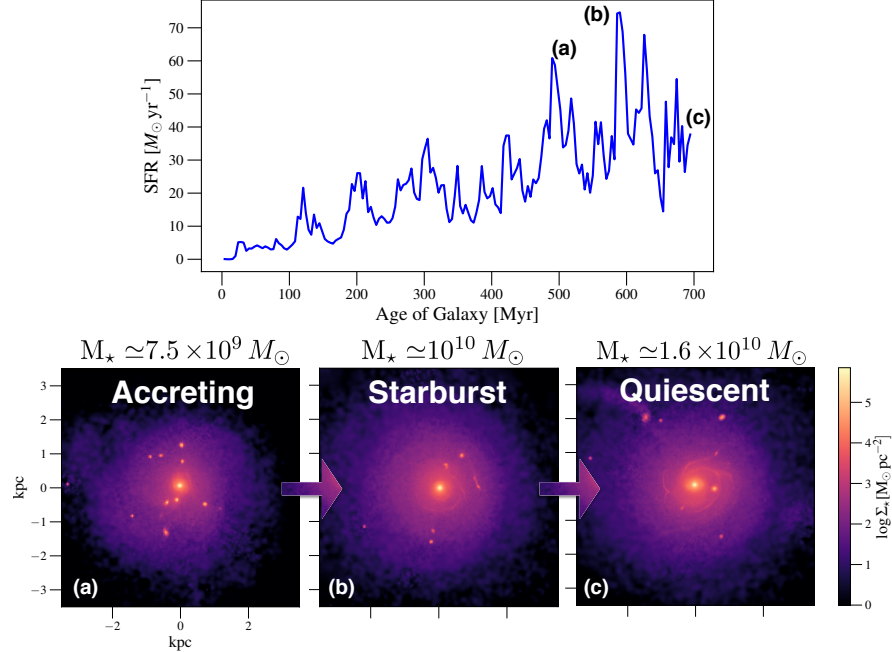


Figure 1. *Top:* Star formation history of Althaea. *Bottom:* projected stellar mass distribution during (a) an early accreting phase; (b) a major starburst following a merger event; and (c) a relatively quiescent post-starburst phase.

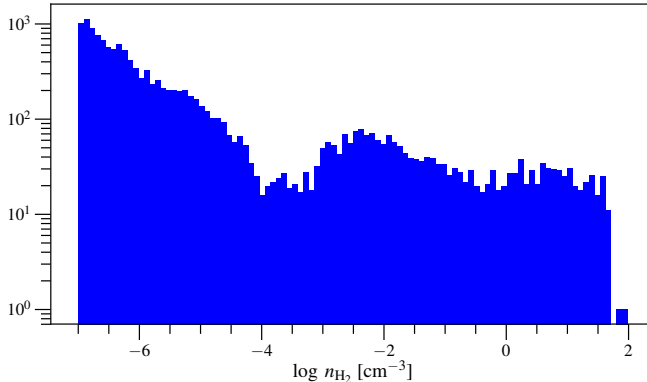


Figure 2. Distribution of molecular gas density of Althaea during the accreting phase shown in Figure 1(b).

applying density cuts to the H_2 density distribution, i.e., MCCs are selected at $n_{\text{cut}} \leq n_{H_2}$. We select 10 equally-spaced cuts in H_2 density in log scale: $(n_{\text{cut}}/1\text{cm}^{-3}) = [0.32, 0.53, 0.88, 1.45, 2.45, 4.08, 6.81, 11.36, 18.96, 31.62]$. Note that with these choice we are including MCCs that are not fully molecular ($n = 0.5n_{H_2}$).

To visually display the clump finding procedure, we overplot the molecular structures identified using a subset of the H_2 density cuts ($n_{\text{cut}} = 0.53, 5.81$, and 18.96 cm^{-3}) on the H_2 density maps (Figure 3). Since the molecular structures are identified in the 3D H_2 density field, they can appear as overlapping structures depending on the viewing angle; thus we also plot them in different projections (right panels of Figure 3) so that the identification can be more easily appreciated. We repeat this identification process for 14 evolutionary stages between redshift $z \in [6.0, 7.2]$, spaced by $\Delta t = 15 \text{ Myr}$.

We impose the additional constraint that an identified struc-

ture must be composed of at least 10 cells. We caution that an important caveat of such a constraint is that we can only examine the parameter space of cloud complexes of radius $R \gtrsim 40 \text{ pc}$, because of the resolution limit of the simulation.

4.2. Molecular Cloud Complex Properties

Upon identifying the molecular structures, we extract properties such as the gas mass M_{gas} , effective size R , Mach number \mathcal{M} , velocity dispersion σ_{gas} , and gas surface density Σ_{gas} to examine their dynamics.

The mass of an MCC is calculated from the uniformly-gridded 3D density field, integrating over the MCC volume V . The effective size is defined assuming spherical geometry, i.e. $R \equiv (3V/4\pi)^{1/3}$. The full velocity dispersion of MCCs is calculated from the bulk velocity field (σ_{bulk}), thermal sound speed (c_s), and the non-thermal velocity dispersion (σ_{NT})

$$\sigma_{\text{gas}}^2 = \sigma_{\text{bulk}}^2 + c_s^2 + \sigma_{\text{NT}}^2. \quad (15)$$

In observations of MCCs, the linewidth contribution of dense gas exceeds that from the diffuse gas. Therefore, when calculating global quantities for MCS, we always perform a mass-weighting. Since we operate on data on a uni-grid, this is equivalent to density averaged quantities. In general, for the quantity x in a MCC we write

$$\langle x \rangle \equiv \frac{\sum_i \rho_i x_i}{\sum_i \rho_i}, \quad (16)$$

where the sum is done for the cells indexed by i composing the MCC. We can use the definition Equation 16 to write each term of the right-hand side of Equation 15 as follows. The bulk velocity dispersion is

$$\sigma_{\text{bulk}}^2 = \frac{1}{3} \langle |\mathbf{v} - \langle \mathbf{v} \rangle|^2 \rangle. \quad (17)$$

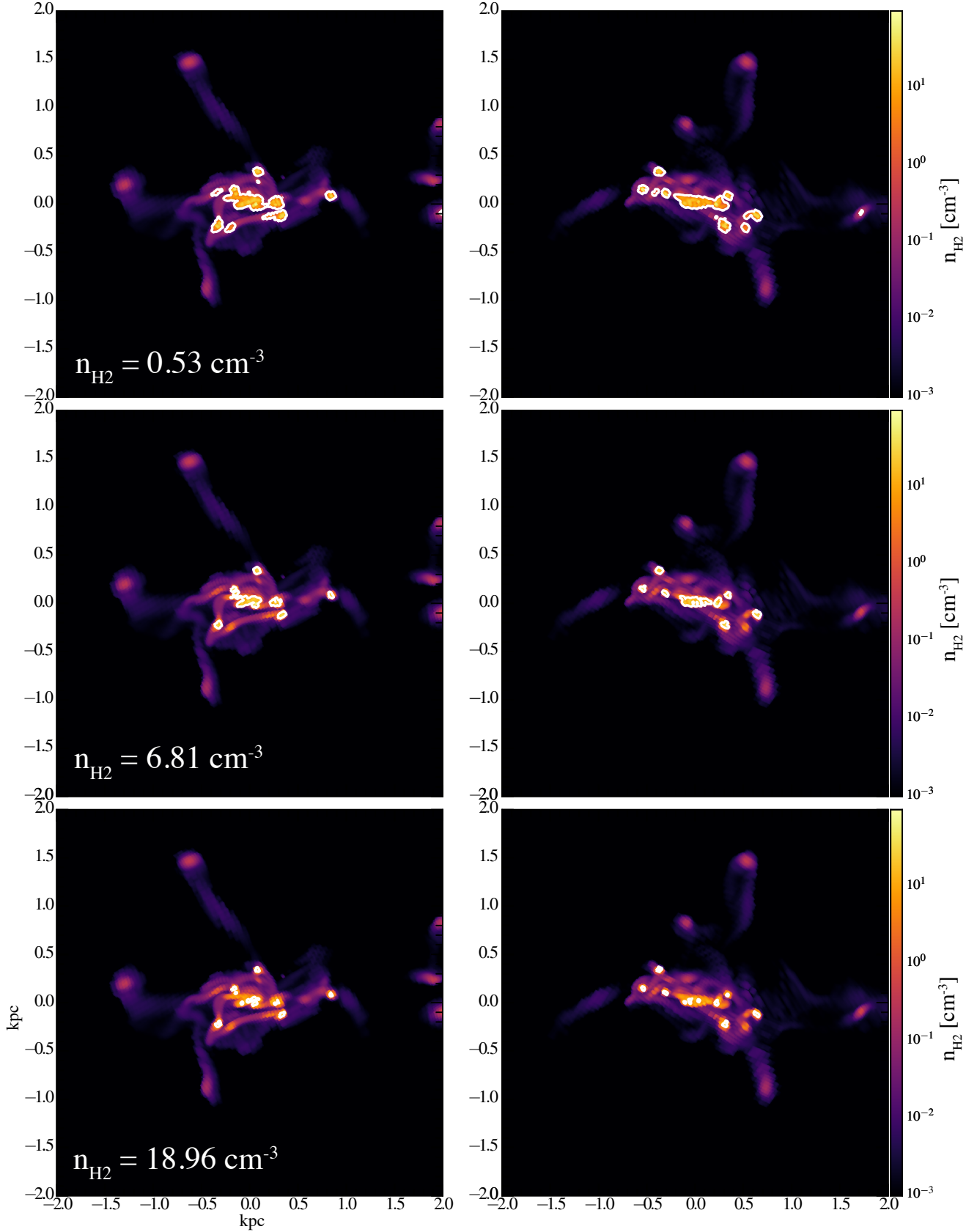


Figure 3. Examples of MCCs (white contours) identified by the clump finder in Althaea during its accreting phase (Figure 1a), where Althaea is dispersion-dominated. Colorbar on the right shows the mean H_2 number density, weighted by gas mass. Different rows show the results obtained by applying different H_2 number density cuts (n_{cut}) as shown by the label. Left and right panels show the galaxy from different viewing angles.

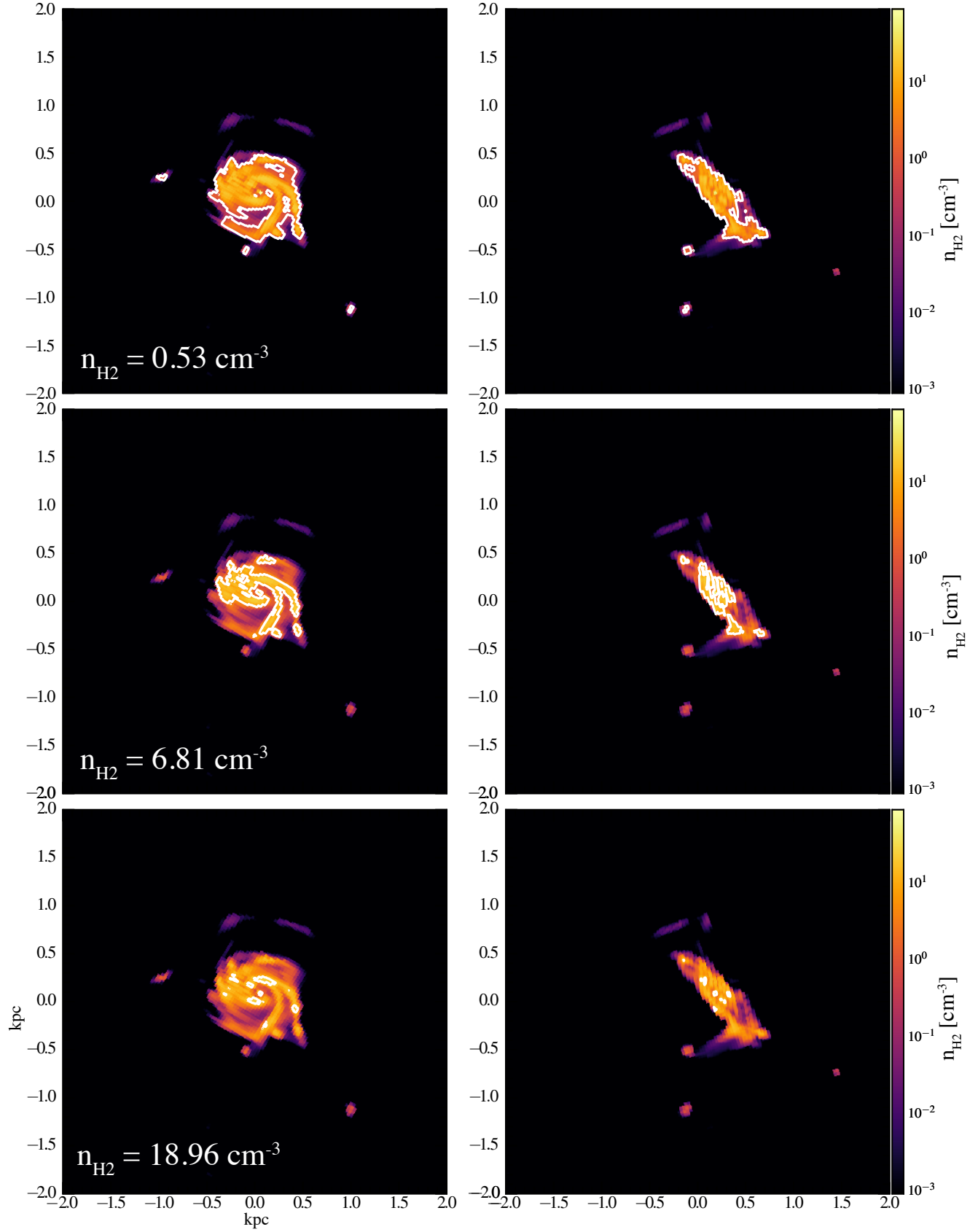


Figure 4. Same as Figure 3, except we show the quiescent phase of Althaea, which is supported by rotation.

The thermal sound speed is calculated from the thermal pressure (P_{TH}) through

$$c_s^2 = \left\langle \frac{k_B P_{\text{TH}}}{m_p n} \right\rangle, \quad (18)$$

where the pressure is in units of K cm^{-3} , k_B is the Boltzmann constant, m_p is the mass of a proton. Similarly, contribution from non-thermal energy is calculated from non-thermal pressure (P_{NT}) as follows

$$\sigma_{\text{NT}}^2 = \left\langle \frac{k_B P_{\text{NT}}}{m_p n} \right\rangle. \quad (19)$$

Finally, the Mach number is related to the pressure terms as follows

$$\mathcal{M} = \left\langle \sqrt{1 + \frac{P_{\text{NT}}}{P_{\text{TH}}}} \right\rangle. \quad (20)$$

5. Results

5.1. Distributions of MCC Basic Properties

We start by considering the MCC distribution in terms of their molecular gas mass, radius, and gas mass fraction, which we define as

$$f_{\text{gas}} = \frac{M_{\text{gas}}}{(M_{\text{gas}} + M_*)}. \quad (21)$$

We show in Figure 5 the results for the distributions considering all the evolutionary stages and dividing the sample in a low ($n_{\text{cut}} = 0.32 \text{ cm}^{-3}$, top panels) and a high ($n_{\text{cut}} = 18.96 \text{ cm}^{-3}$, lower panels) density cuts¹⁰. Overall, the mass of all MCCs identified ranges between $M_{\text{gas}} \simeq 10^{5.5-8.5} M_\odot$, which is comparable to those observed in $z \sim 2$ galaxies in rest-frame UV and optical light (Elmegreen et al. 2007, 2009). The gas fraction ranges from $f_{\text{gas}} \simeq 0.1 - 100$ over all the MCCs identified across all evolutionary stages of Althæa. The most massive ($M_{\text{gas}} > 10^8 M_\odot$) cloud identified at each density threshold corresponds to the molecular disk of the galaxy, which is identified as a single component for low n_{cut} . This main disk component occupy the top right corner of Figure 6 has a (AP: do we really need both f_{gas} and M_*/M_{gas} ?) stellar-to-gas mass ratio of $\simeq 50-100$.

5.2. Single Evolutionary Stage

We can now focus on the two most extreme evolutionary stages of Althæa — the accreting and starburst phases (see §3.1). Scaling relations for the MCCs identified are shown in Figure 7 for the accreting (left panels) and starburst phase (right panels), respectively.

During the accreting phase, MCCs in Althæa are characterized by large velocity dispersions ($\sigma \simeq 100 \text{ km s}^{-1}$) and sizes ($R \simeq 100 \text{ pc}$). These values are comparable to those

¹⁰ The highest density threshold of $n_{\text{cut}} = 31.62 \text{ cm}^{-3}$ corresponds to a minimum MCC mass of the order of $10^{5.5} M_\odot$ for the densest structure. However, not all evolutionary stages considered have at least one MCC at this highest density threshold, we therefore consider MCCs identified with the second highest density threshold ($n_{\text{cut}} = 18.96 \text{ cm}^{-3}$).

found in starburst galaxies, such as the nearby gas-rich galaxy M64 and the $z \sim 2$ starbursting disk galaxy SMM J2135-0102 (Rosolowsky & Blitz 2005; Swinbank et al. 2011), but are higher than those found in the Milky Way and extragalactic GMCs by an order of magnitude (Heyer & Brunt 2004; Bolatto et al. 2008).

While the virial parameter defined as Equation 5 is typically used in observational studies, as they are designed to probe structures that are composed of mainly molecular gas only, we calculate the virial parameter of MCCs including the influence from the stellar component (i.e., $\alpha_{\text{vir,tot}}$ via Equation 6) given the high stellar-to-gas mass ratios of some of them (see Figure 6). MCCs with the highest (AP: do we really need both f_{gas} and M_*/M_{gas} ?) stellar-to-gas mass ratio ($\gtrsim 1$) correspond to the central main disk of Althæa (see top panels of Figure 3 and Figure 4, see also §4.2), which includes a large fraction of stellar mass that are already assembled in Althæa. This explains the low total virial parameter seen in the most massive MCCs of Althæa in this phase, as shown in the middle left panel of Figure 7, where the stellar gravitational potential influence the overall stability of such MCCs.

Motivated by observational studies, we also plot the σ_{gas}^2/R ratio and gas surface density of MCCs in the bottom left panels of Figure 7. In the same plot, we show those observed in the Galactic Ring Survey (GRS) of the Milky Way (Heyer et al. 2009) for comparison. Dashed lines in the figure show the loci along which the annotated external pressures are needed for any molecular clouds in equilibrium to have certain linewidths for a given set of surface densities (see §2.1).

In the starburst phase, MCC have similar velocity dispersion and sizes as those in the accreting phase; however, the MCCs in the starburst phase span a wider range in gas surface density (bottom panels of Figure 7) and have lower virial parameters, i.e. they more susceptible to collapse. Due to a time delay between cloud collapse and star formation, we also compare the virial parameter of MCCs in the pre-starburst phase and post-starburst phase Figure 8 shows that most MCCs in the pre-starburst phase have even lower virial parameter than in the starburst phase. On the other hand, the virial parameter of MCCs in the post-starburst phase is higher than in both the pre-starburst and the starburst phase. This is consistent with our physical intuition of gas instability leading to star formation.

5.3. Adopted Density Threshold Dependence and Temporal Evolution

We investigate possible variations in the dynamics of the molecular structures of Althæa to test the robustness of our results against the choice of density threshold by adopting different sets of n_{cut} in identifying the MCCs. That is, how sensitive are the structure properties, and thus, the results presented in §5.2 dependent on the choice of density thresholds.

The sizes of MCCs are dependent on the choice of n_{cut} , and thus, some of the MCCs within the main disk break into mul-

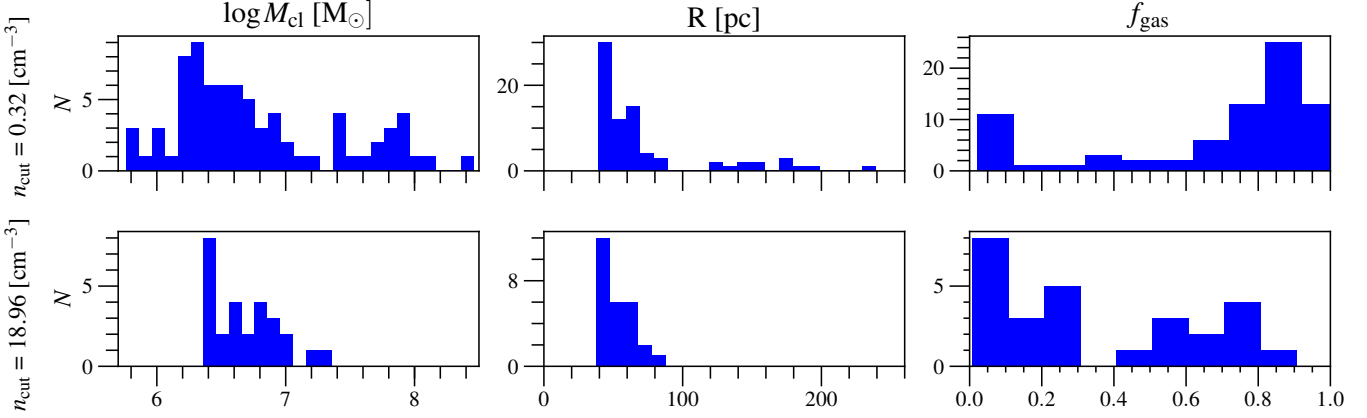


Figure 5. Distributions of mass (left), size (middle), and gas mass fraction (right) of MCCs identified using the lowest n_{cut} (top panels) and $n_{\text{cut}} = 18.96 \text{ cm}^{-3}$ (bottom panels) over all the considered evolutionary stages. Note that the scales shown on the y-axes are different between the top and bottom panels, as fewer MCCs are identified at higher n_{cut} .

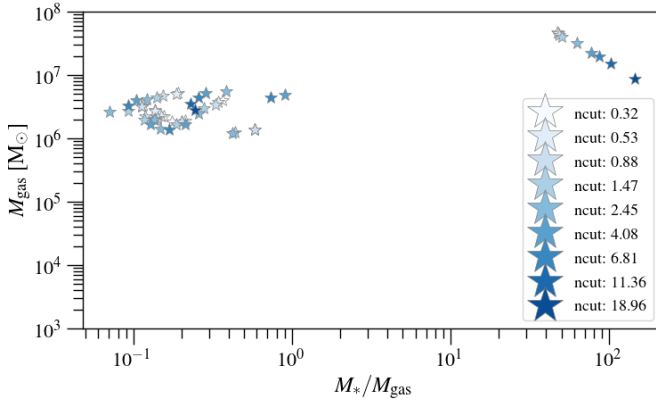


Figure 6. Cloud mass and stellar-to-gas mass ratio of MCCs identified in the accreting phase of Althaea. The most massive MCCs have the highest stellar-to-gas mass ratio ($\gtrsim 1$) (AP: **do we really need both f_{gas} and M_*/M_{gas} ?**) as they correspond to a large part of Althaea, and thus, include a large number of stellar mass that is already ensembled in Althaea

multiple sub-MCCs at higher n_{cut} . The cluster of points found at the lowest density threshold, occupying the top right corner of the linewidth-size relation in the top left panel of Figure 9, are broken down into sub-MCCs at the highest density threshold (see top right panel of the same figure¹¹). These sub-MCCs are smaller in size, and thus, are shifted leftward in the top right panel. In this way, we identify a population of denser molecular structures (see Figure 3).

We note that similarly massive molecular structures (few times $10^7 M_{\odot}$ ¹²) have been reported in idealized closed-box isolated galaxy simulations done at higher resolution (e.g., a maximum resolution of 3 pc in the 48 kpc box studied by Behrendt et al. 2016). However, the IGM and merger and accretion histories are not properly modeled in such simulations since they adopt non-cosmological initial conditions. That said, the similar mass range found in MCCs of Althaea is reassuring — our results are not far off in spite of the limited

¹¹ Note that while the biggest MCCs are broken into sub-MCCs at higher n_{cut} , MCCs identified at lower density in the outskirts of Althaea typically do not reach the density thresholds as n_{cut} increases. Hence, there are fewer MCCs at the highest density threshold.

¹² See §3.1 of Behrendt et al. (2016).

resolution ($l_{\text{cell}} \simeq 30 \text{ pc}$). The gas velocity dispersion σ_{gas} is rather insensitive to the actual value of n_{cut} . This lack of variation is reassuring. Our inference on the dynamics of $z \sim 6$ MCCs in relation to those observed in nearby and $z \sim 2$ galaxies in the context of linewidth-size relation is thus not artifacts or biased by our choice of n_{cut} in this work.

We show the properties of all MCCs identified across all evolutionary stages in Figure 9. One of the most pronounced differences in the dynamics of MCCs traced over the 700 Myr shown in this work is seen in the virial parameter — the most relevant phases are shown in Figure 8 (see §5.2).

6. Discussions and Implications

6.1. Comparing MCC Observable Quantities to Observations

In this section, we compare the observable quantities of MCCs obtained from the simulations (e.g., σ_{gas} , R , M_{gas} , Σ_{gas}) with those of molecular gas structures from observations at lower redshift. We exclude for the moment the biggest MCC identified in each evolutionary stage, which correspond to the main disk of Althaea (i.e., the top right cluster of points in the linewidth-size relation of Figure 7 and the top left panel of Figure 9).

The MCCs of Althaea have dynamics largely similar to those observed in $z \sim 2$ spatially resolved studies of gas-rich star-forming galaxies, in terms of their velocity dispersions, sizes, and gas surface densities (Figure 7; see e.g., Swinbank et al. 2011), with sizes of the order of $R \simeq 100 \text{ pc}$ and velocity dispersions of $\sigma_{\text{gas}} \simeq 20\text{--}80 \text{ km s}^{-1}$. Their velocity dispersions are also comparable to those observed in the inner Milky Way and nearby gas-rich galaxies (e.g., M64; Oka et al. 2001; Rosolowsky & Blitz 2005; Heyer et al. 2009), which lies along the locus of $\sigma_{\text{gas}} \propto R^{0.56}$. Such high velocity dispersions and surface densities can be explained partly because these MCCs are located in the nuclear regions of the galaxy, where the potential well is the deepest, and also from the injection of kinetic energy from recent star formation as Althaea is assembling its stellar mass (given the high Mach

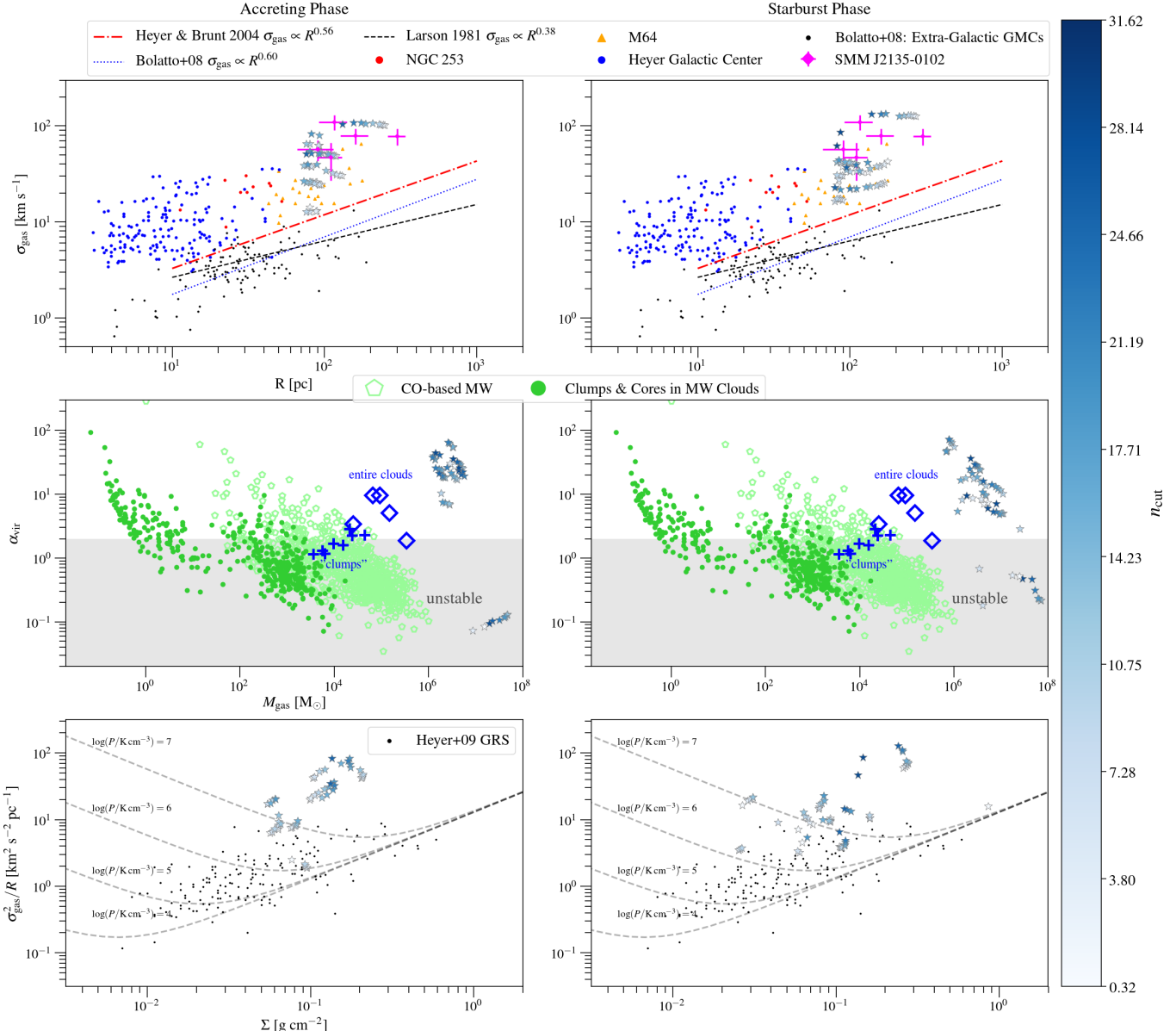


Figure 7. Linewidth-size relation (top), α_{vir} -mass relation (middle), and σ^2/R - Σ_{gas} relation (bottom) for MCCs (star symbols) identified in the two most extreme evolutionary stages of Althaea — accreting phase (left) and starburst phase (right). Star symbols are color-coded by the density thresholds n_{cut} , as illustrated by the colorbar. Literature data in the linewidth-size plots are from Heyer & Brunt (2004); Rosolowsky & Blitz (2005); Bolatto et al. (2008); Leroy et al. (2015), and Swinbank et al. (2011), and the empirical scaling relations are from Larson (1981); Heyer & Brunt (2004); Bolatto et al. (2008). Data points in the α_{vir} -mass figure are taken from Kauffmann et al. (2017a) and Kauffmann et al. (2017b) and references therein (see Fig 4 of Kauffmann et al. 2017b). The gray dotted lines shown in the bottom panels correspond to the various external pressures for gas in equilibrium, see Equation 3.

numbers of MCCs; §4.2). In fact, by the accreting stage (see Figure 1a) at $z \approx 7.2$, Althaea has assembled a stellar mass of $M_{\star} = 7.5 \times 10^9 M_{\odot}$. (**AP: I do not fully understand the following**) Furthermore, the comparison of the velocity dispersion from bulk motions versus that from turbulence (Figure 10) suggests that the high total velocity dispersion seen in the MCCs of Althaea is partly a result of large-scale rotation, which is even more important in its later stage of evolution as Althaea is settling into a rotating disk galaxy. The implication of this in interpreting observational results is further discussed in the next subsection (§6.2).

The high pressure observed in Althaea (see Pallottini et al.

2017a) is comparable to what has been observed in local ultra-luminous IR galaxies (ULIRGs); however, the molecular clouds in the latter are concentrated within their central regions and have typical sizes of ~ 70 -100 pc and masses on the order of $\sim 10^9 M_{\odot}$ (Downes & Solomon 1998; Sakamoto et al. 2008). In our simulated galaxy, the high pressure MCCs of Althaea are found throughout the disk. This difference likely stems from the different physical mechanisms giving rise to the formation (and thus the nature) of these molecular structures. In local ULIRGs, MCCs are likely formed by shock compression and cloud-cloud collisions that funnel large amounts of gas from the progenitor galaxies towards the

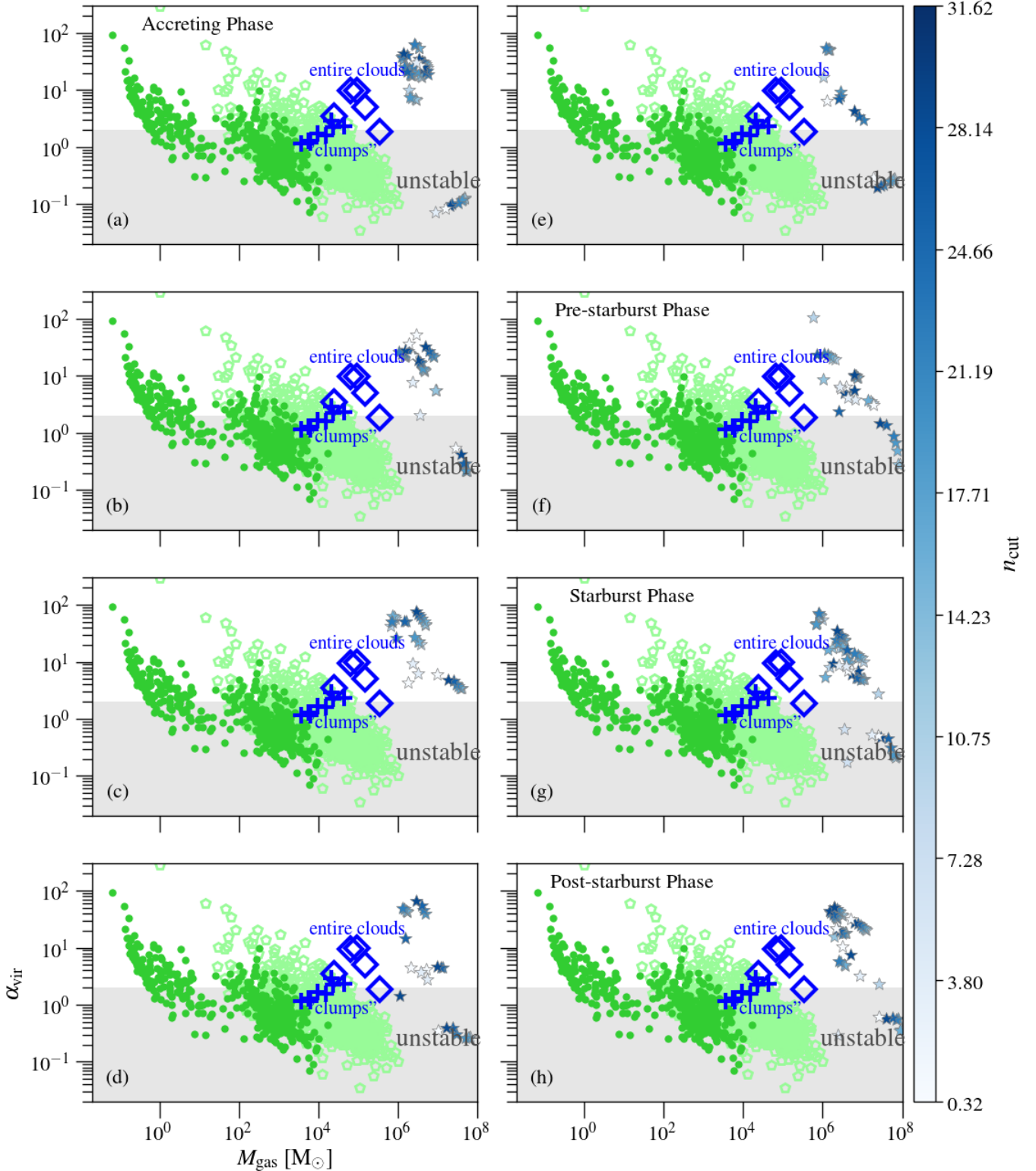


Figure 8. Virial parameter as a function of MCC mass for different evolutionary stages of Althaea, beginning from the accreting phase (top left). Evolutionary stages are shown chronologically from panels (a) through (f). Definition of symbols are same as in Figure 7. Blue star symbols show gas-only α_{vir} and blue circulate dots show total $\alpha_{\text{vir,tot}}$. The virial parameter vary over the ~ 300 Myr shown here as Althaea evolves. Most notably, the biggest MCCs transition from the unstable region as Althaea accretes materials to being stable (e.g., panel (c)), a similar pattern is seen in the pre-starburst through post-starburst phase. The variation is clearly seen between the pre-starburst through post-starburst phase. Excluding the biggest MCCs (see Figure 6 and §5.2), MCCs in the pre-starburst phase have a lower α_{vir} compared to the starburst phase. (**AP: I still think that this figure might be a bit redundant**)

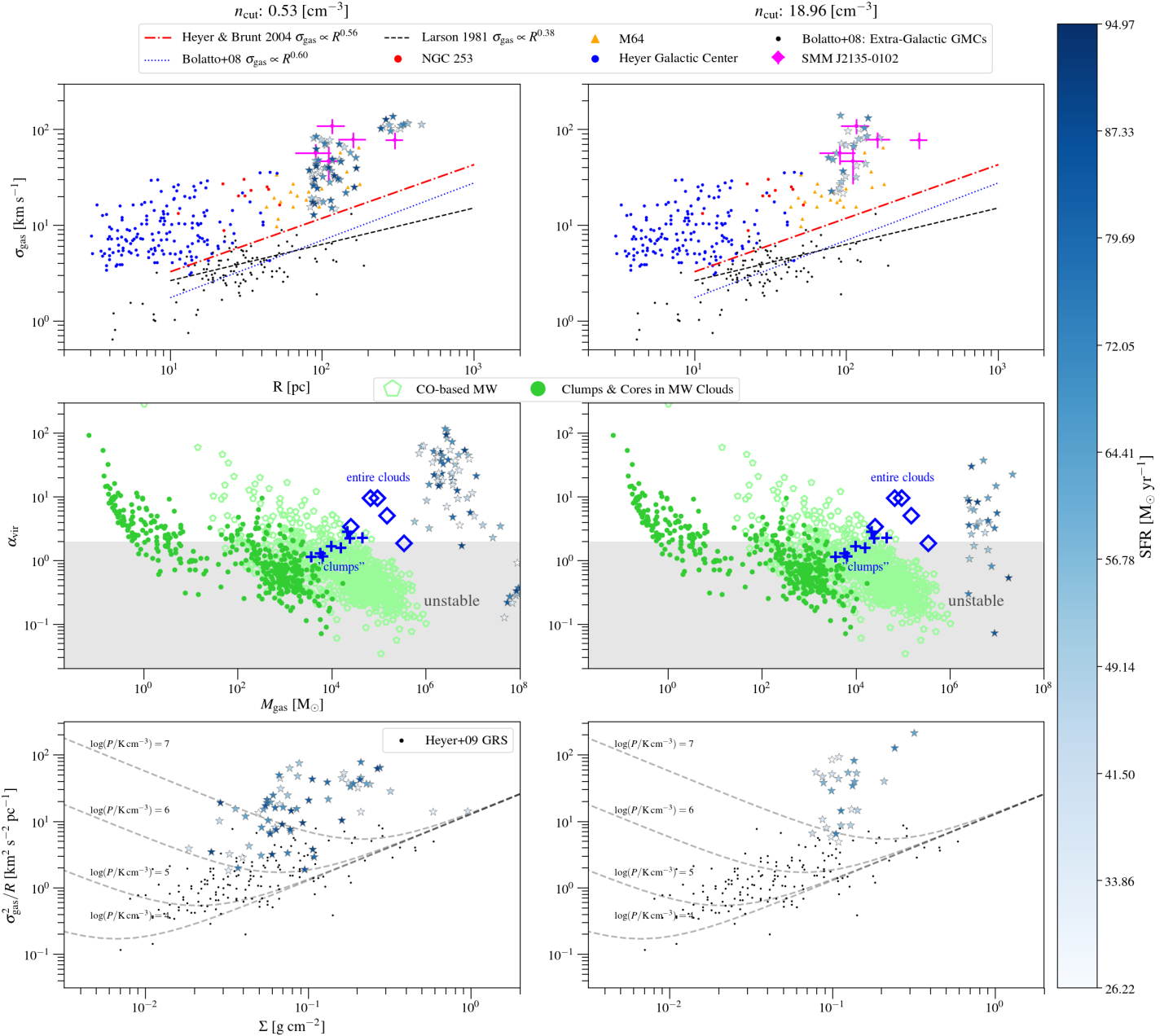


Figure 9. Same as Figure 7, except star symbols are showing MCCs identified across all evolutionary stages traced in our simulation, which are color-coded by the SFR of Althaea in those stages (see colorbar). Left panels show MCCs identified using a low density threshold of $n_{\text{cut}} = 0.53 \text{ cm}^{-3}$ and right panels show MCCs identified using a high density threshold of $n_{\text{cut}} = 18.96 \text{ cm}^{-3}$. The biggest MCCs identified at lowest density threshold, occupying the top right corner of the top left panel), are broken into smaller MCCs at higher density thresholds (top right panel).

central region (Tan 2000; Wu et al. 2018). On the other hand, the highly turbulent structures of Althæa are the result of extra-planar flows (Kohandel et al., in prep. 2019) and higher velocity accretion/SN-driven outflows (Gallerani et al. 2018). The presence of extra-planar flows may also be the dominant mode for forming the highly supersonic massive MCCs observed in gas-rich star-forming galaxies at $z \sim 2$ (see also e.g., Swinbank et al. 2011) — but the observed size scales could also be biased high due to the resolution limit.

In terms of the Larson’s linewidth-size relation, we do not find any major quantitative differences in the MCC properties with respect to those observed in the nearby Universe between the accreting and starburst phase of Althæa (see Figure 7), which are separated by $\simeq 300$ Myr. However, MCCs in the pre-starburst phase have lower α_{vir} compared to the starburst phase. Similarly, the virial parameter is higher in the post-starburst phase compared to both the pre-starburst and starburst phases. This is expected for star formation to proceed.

6.2. Importance of Bulk Motions in Measured Velocity Dispersion

The local sound speed of all identified molecular complexes is typically much smaller than their non-thermal (turbulent) velocities, as non-thermal pressure dominates thermal pressure for dense gas (Pallottini et al. 2017b), i.e. $c_s^2 \ll \sigma_{\text{NT}}^2$. In particular, the Mach number averaged on the the MCCs distribution at the highest density threshold is $\mathcal{M} \simeq 6$; this is consistent with the analysis done in (Vallini et al. 2018), that finds a global Mach number of $\mathcal{M} \sim 10$ for Althæa. This can be further analyzed as follows. In Figure 10 we show the gas velocity dispersions from bulk motions versus turbulent motions for MCCs in the accreting and quiescent phase. Recall that Althæa displays a disturbed morphology in the accreting phase but a disk-like morphology in the quiescent phase (see Figure 3 and Figure 4). Most MCCs in the accreting phase have turbulent velocity dispersions higher than the bulk motion velocity dispersions, whereas the opposite is true in the quiescent phase. In addition, the two velocity dispersion terms are of the same order of magnitude. (DL: interpretation To be revised ...) (AP: I still do not get the point; bulk motion is a dispersion, i.e. should not receive contribution from the rotation of the system; a possibility might be to calculate the specific angular momentum ($\vec{x} \wedge \vec{v}$ averaged using Equation 16) of the system and compare it to the one for gas in circular motion) This indicates that gas velocity dispersions observed on similar physical scales and resolutions as presented here have an important contribution from large-scale rotation. Hence, the linewidths observed in high- z molecular gas structures on these scales should *not* be taken as a direct evidence they are intrinsically more turbulent than those in the local ISM, and the comparison and interpretation of the dynamics of gas structures with local clouds using e.g., the Larson’s relations is non-trivial. Behrendt et al. (2016) draw a similar conclusion using pc-scale resolution simula-

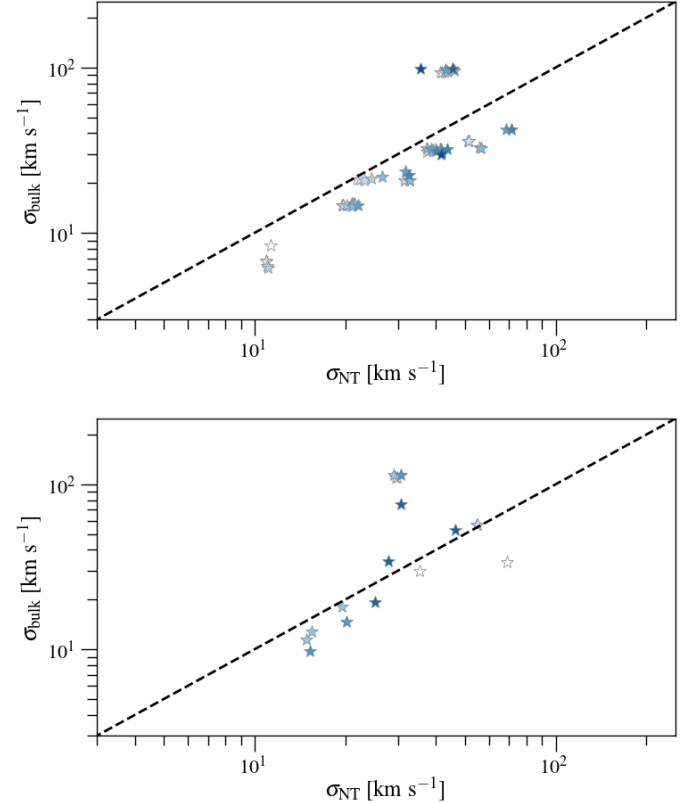


Figure 10. Gas velocity dispersions from bulk motions and turbulent motions of Althæa in accreting (top) and quiescent phase (bottom). The accreting phase (Figure 3) displays a more disturbed morphology compared to the quiescent phase, which displays a disk-like morphology (Figure 4). The velocity dispersion from turbulent motions is higher than that from bulk motions for most MCCs in the accreting phase, but the opposite is true in the quiescent phase. Thus, large-scale motion plays an important role in contributing to the total velocity dispersion. This implies that the velocity dispersion measured in molecular gas structures from observations on similar physical scales should not be taken as direct evidence that these structures at high redshifts are intrinsically more turbulent than those in the local ISM.

tion: large-scale bulk motions may mimic turbulent velocity dispersion due to beam smearing.

6.3. Toomre Parameter and Stability of MCCs

We define Toomre Q parameters for the gas, stars, and the effective two-component Q_{eff} in §2.2. Maps of the corresponding Toomre Q are shown in Figure 12 (see also Figure 2 for example of MCCs identified in this evolutionary stage of Althæa using different n_{cut}).

Close resemblance of the Q_{eff} and Q_{\star} maps indicates that contributions from the stellar component play an important role in governing the stability of the MCCs against perturbations. This can be understood since stars in Althæa dominates the central part of the galaxy in mass, so their gravitational potential provides a non-negligible contribution to the instability. Similarly, contribution from the thickness of the disk is important in Althæa since its disk is warped and has a scale height-to-radius ratio of $h/r_{\text{gal}} \sim 150 \text{ pc}/1 \text{ kpc} \simeq 0.15$.

That is, some MCCs are found in regions of $Q_{\text{gas}} \sim 1$, which is consistent with the expectation that they correspond to regions of high surface densities that are gravitationally unsta-

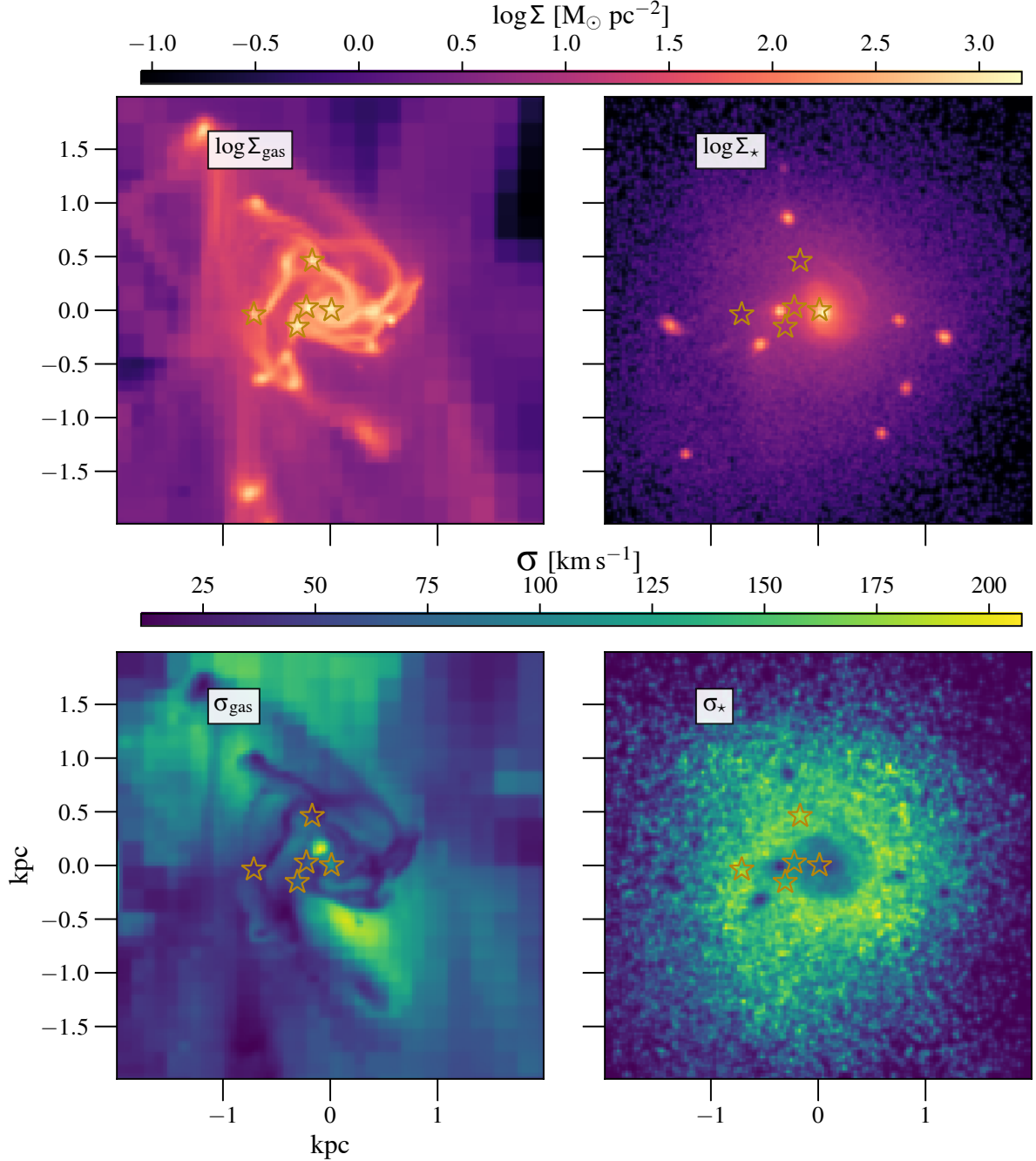


Figure 11. Surface density maps of the gas (top left) and stellar (top right) components of Althaea (accreting phase) and their radial velocity dispersion maps projected onto the xy -plane (bottom panels). Center of mass positions of MCCs within ~ 1.5 kpc of Althaea identified with $n_{\text{cut}} = 6.81 \text{ cm}^{-3}$ are overplotted as star symbols as an illustrative example.

ble. Note, however, that when including the stabilizing effects due to the stellar potential of Althaea and the thickness of its disk (via σ_z , i.e., Q_{eff} ; see Equation 13), some of these MCCs are consistent with $Q_{\text{eff}} > 1$. This demonstrates the importance of accounting for stellar contribution and disk thickness when examining the stability of molecular gas structures. This consideration is especially relevant for the relatively evolved and enriched systems at high redshift, that are preferentially being imaged at high resolution with ALMA. In the outer regions of Althaea, on the other hand, Q_{eff} resembles Q_{gas} , with

both $\log Q_{\text{gas}}$ and $\log Q_{\text{eff}} < -1$. Notably, these are the more gas-rich regions (see Figure 11).

The large virial parameters seen in some MCCs of Althaea can be understood by first noting that fragmentation *can* happen in regions of low Q (if we only consider instability against axisymmetric perturbations), but further evolution/collapse depends on the dynamics or equation of state of the gas. Such fragmentation is expected to take place at the critical scale length $\lambda_{\text{crit}} < 2\pi^2 G\Sigma/\kappa^2$. Second, this fragmentation scale is greater than the typical size of GMCs. This could be in-

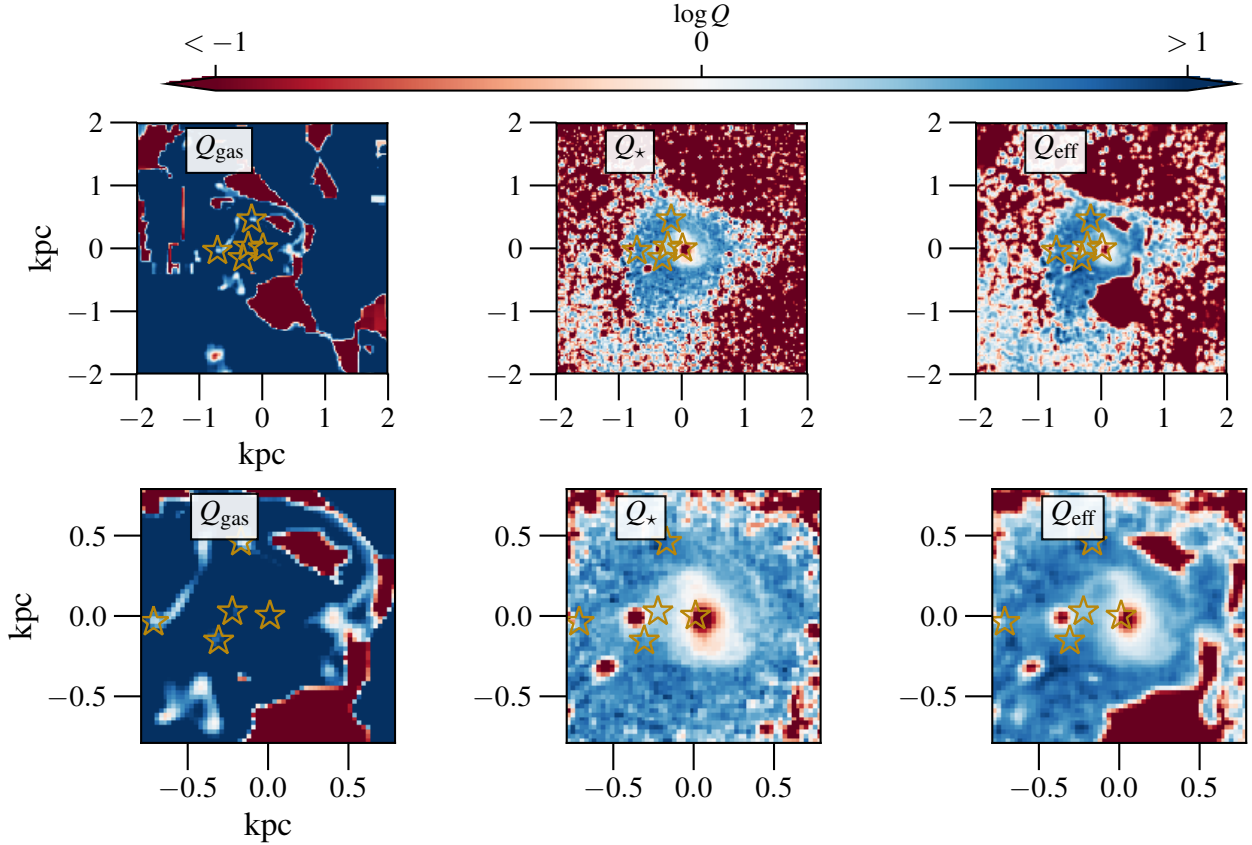


Figure 12. Toomre Q maps derived from the central $r=2$ kpc (top row) and $r=0.8$ kpc (bottom row) of Althaea. Gas-only Q_{gas} is shown in the left panels and stellar-only Q_{\star} is shown in the middle panels. Maps of the effective two-component Q_{eff} parameter are shown in the right panels. All maps are projected onto the xy -plane. Positions of MCCs identified with $n_{\text{cut}} = 6.81 \text{ cm}^{-3}$ are overplotted as star symbols. A smoothing length of 30 pc has been applied to the maps. A divergent colormap is used for the Toomre Q maps to facilitate identification of regions above and below $\log Q=0$. Some MCCs lie in regions of $\log Q_{\text{eff}} \gtrsim 0$, where regions of $\log Q_{\text{eff}} \lesssim 0$ are likely gravitationally unstable. Close resemblance of the Q_{\star} and Q_{eff} maps in the central region of Althaea indicates that the stellar component plays an important role in governing the stability of the MCCs against $m=0$ perturbations, highlighting the importance of accounting for stellar contribution when examining the stability of molecular gas in relatively evolved and enriched systems at high redshifts. (AP: maybe it is better to put a single set of maps, with FOV from -1.5 to 1.5 kpc)

terpreted as a result of instability setting the scales for fragmentation, *but the truly star-forming regions correspond to the collapsing, denser, and cooler molecular structures that are on smaller scales*. Thus, the high virial parameter found for some MCCs in Althaea indicates that they are not the collapsing structures and are found in regions of $Q_{\text{eff}} > 1$. On the other hand, MCCs in (the denser) regions with a lower Toomre Q_{eff} parameter are unstable and star formation is expected to take place within its star-forming *clumps* and *cores* on smaller scales, where energy quickly dissipates.

If most of the MCCs in Althaea are stable against collapse, how does it sustain its high SFR of $\sim 70 M_{\odot} \text{ yr}^{-1}$ in the starburst phase? Such tension in the interpretation is understood as follows. First, due to turbulence dissipation on small-scales, such (sub-)structures are no longer supported by differential rotation. This in turn enables sub-regions of the MCCs to collapse and potentially form OB associations out of these unbound MCCs (Clark & Bonnell 2004; Clark et al. 2005). Further, the SFR of Althaea is very bursty and high SFR stages are only transient. Finally, our results are limited by the resolution of the simulation, i.e., in Althaea we do not resolve star

formation in *cores* and *clumps* as in the classical molecular cloud hierarchy. This re-iterates the statement about low Q above.

7. Summary and Conclusions

Properties of the star-forming ISM of galaxies near the Epoch of Reionization are now within reach with ALMA. While it is possible to obtain sensitive and high fidelity imaging that reveals their gas and dust morphology on sub-kpc scales and even smaller, such observations remain time-consuming; logically, data from multiple cycles pushing to increasing resolution and sensitivity are needed. As such, observational studies on such scales are still missing in the literature. In this work, we aim to understand the origin and dynamical properties of molecular clouds complexes in prototypical galaxies at the EoR in numerical simulations to provide a framework within which upcoming observations can be compared against to aid in the interpretation.

We study the dynamics of MCCs in a $z \sim 6$ prototypical galaxy, Althaea, and their temporal evolution using the state-of-the-art cosmological zoom-in simulations (SERRA), which include a chemical network to determine the forma-

tion of molecular hydrogen, heating and cooling of the ISM by UV radiation and metal lines, and detailed stellar feedback. Properties of Althæa are briefly summarized in §3. We use a three-dimensional clump-finding algorithm to identify MCCs. We decompose the molecular structures into non-overlapping objects by identifying a set of density contours with varying densities at multiple evolutionary stages. Most notably, the accreting phase, starburst phase, and quiescent phase. We extract properties such as mass, size, Mach number, velocity dispersion, gas surface density, and virial parameter ($M_{\text{gas}}, R, \mathcal{M}, \sigma_{\text{gas}}, \Sigma_{\text{gas}}, \alpha_{\text{vir}}$) for each MCC and perform a Toomre- Q stability analysis on Althæa.

The sizes of MCCs are dependent on the choice of n_{cut} , and thus, some of the MCCs within the main disk break into multiple sub-MCCs at higher n_{cut} . The ~ 200 pc-scale MCCs found with a low density threshold correspond to the arms of the disk of Althæa and break down into smaller $\lesssim 100$ pc-scale MCCs at higher density thresholds. Overall, the mass of MCCs ranges between $10^{5.5-8.5} M_{\odot}$, depending on the chosen density threshold. This mass range is comparable to those observed in $z \sim 2$ galaxies in rest-frame UV and optical wavelengths. Similarly massive molecular structures (few times $10^7 M_{\odot}$) have been reported in idealized closed-box isolated galaxy simulations done at higher resolution (e.g., $l_{\text{cell}} \simeq 3$ pc in the 48 kpc box studied by Behrendt et al. 2016). However, the IGM and merger and accretion histories are not properly modeled in such simulations. That said, the similar mass range found in MCCs of Althæa is reassuring — our results are not far off despite the resolution limit ($l_{\text{cell}} \simeq 30$ pc). On the other hand, the gas velocity dispersion σ_{gas} is rather insensitive to the adopted density threshold.

We compare several observable quantities that reflect the dynamics of MCCs in Althæa to those observed in the Milky Way disk, the Galactic center, and gas-rich starburst galaxies in the local Universe, and at the peak epoch of cosmic star formation in the context of the Larson’s relations. This comparison is done for different evolutionary stages of Althæa.

MCCs of Althæa are found to have velocity dispersion and gas surface density systematically higher than Milky Way clouds regardless of the density threshold n_{cut} adopted. These MCCs are, in fact, highly supersonic (with high Mach numbers). Their velocity dispersions are comparable to those observed in $z \sim 2$ starburst galaxies ($\sigma_{\text{gas}} \simeq 200$ km s $^{-1}$); (**DL:** **TBD**) however, comparing the velocity dispersions of MCCs from bulk motions versus turbulence indicates that large-scale rotation is an important contributor, even in the accreting phase of Althæa, which displays a highly disturbed morphology. This poses a challenge to the interpretation of spatially resolved molecular gas structures observed in high- z galaxies to-date. In particular, any velocity dispersions measured on similar scales as here (even down to ~ 40 pc) should *not* be taken as a direct evidence that high- z molecular gas structures are intrinsically more turbulent than those in the local ISM, unless contributions from bulk motions are properly ac-

counted for.

Close resemblance of Q_{eff} and Q_{star} maps indicates that contributions from the stellar component play an important role in governing the stability of the MCCs against axisymmetric perturbations, especially in the central part of Althæa. Similarly, stabilizing effect due to the thickness of its disk is also non-negligible. Our Toomre- Q analysis thus illustrates the importance of accounting for stellar contribution and disk thickness when examining the stability of molecular gas structures, especially in relatively evolved and enriched systems at high redshift that are preferentially being observed now.

We perform virial analysis, as motivated by observations, where the virial parameter is used as a surrogate to comparing the potential to kinetic energies of molecule gas structures. The high virial parameter found for some MCCs in Althæa indicates that they are not the collapsing structures and are found in regions of $Q_{\text{eff}} > 1$. On the other hand, MCCs in (the denser) regions with a lower Toomre Q_{eff} parameter are unstable and star formation is expected to take place within its star-forming *clumps* and *cores* on smaller scales, where energy quickly dissipates. This is consistent with the notion that collapsing structures result from gravitational instability occurring within globally stable structures, which are supported by turbulence and rotation on large scale. This also implies observations on spatially resolution better than $\simeq 40$ pc are needed to examine the truly star-forming structures (cores), and thus, star formation in the first galaxies.

We examine temporal variations in the MCC dynamics over the course of 700 Myr traced in our simulation. One of the most prominent differences is the virial parameter, which is the lowest in the pre-starburst phase but increases after a starburst as gas is self-regulated by feedback.

Determining the multi-phase ISM properties of early galaxies is a critical piece to understanding the evolution and assembly history of galaxies, since they set the pace for chemical reactions and excitation rates for the coolants in the ISM (and subsequent star formation). While observations leveraging the combination of spatial-spectral imaging of multi-band continuum and spectral line emission are crucial, we show in this work that prototypical galaxies at the EoR with properties similar to Althæa are expected to have molecular gas structures on sub-kpc scales; however, these are not the truly star-forming regions. The linewidth of molecular gas structures probed on these scales partially results from large-scale motions even in a highly disturbed stage. This means that caution should be taken when interpreting observational data, albeit the impressive resolution and sensitivity that are unprecedented. Thus, with the resolution provided by existing data, it remains unclear whether high- z molecular gas structures are truly intrinsically more turbulent than those in the local ISM. This picture will become clearer as deeper and higher resolution imaging of molecular gas at high- z are obtained with ALMA and Northern Extended Millimeter Array (NOEMA) in the next few years, and potentially with the Next Gener-

ation VLA (ngVLA) in the 2030s. On the other hand, cosmological zoom-in simulations, such as SERRA, while inherently limited in galaxy statistics and are subject to the sub-grid models adopted, serve as a useful tool for examining and making predictions on the morphology and dynamics of the molecular ISM of the first galaxies.

Acknowledgements

We thank Jens Kauffmann, Thushara Pillai, and Mark Swinbank for sharing their data, and Jens for useful discussions. TKDL acknowledges support by the NSF through award SOSPA4-009 from the NRAO and support from the Simons Foundation. AF acknowledges support from the ERC Advanced Grant INTERSTELLAR H2020/740120. M-MML acknowledges partial support by the NSF through award AST18-15461, and hospitality from the Institute for Theoretical Astrophysics at the University of Heidelberg. This work

is based on a project developed at the Kavli Summer Program in Astrophysics (KSPA) held at the Center for Computational Astrophysics of the Flatiron Institute in 2018. The program was co-funded by the Kavli Foundation and the Simons Foundation. We thank the KSPA Scientific and Local Organizing Committees, and the program founder, Pascale Garaud, for supporting the genesis of this work. We also thank the Center for Cosmology and Particle Physics at the New York University for their hospitality in hosting us after the steam pipe explosion in NYC during the KSPA. This research has made use of NASA’s Astrophysics Data System Bibliographic Services. We acknowledge use of the Python programming language (Van Rossum & de Boer 1991), Astropy (Astropy Collaboration et al. 2013), Cython (Behnel et al. 2011), Matplotlib (Hunter 2007), NumPy (van der Walt et al. 2011), PYMSES (Labadens et al. 2012), SciPy (Jones et al. 2001–), and YT (Smith et al. 2009; Turk et al. 2011).

-
- Agertz, O., Kravtsov, A. V., Leitner, S. N., & Gnedin, N. Y. 2013, *ApJ*, **770**, 25
- Astropy Collaboration, Robitaille, T. P., Tollerud, E. J., et al. 2013, *A&A*, **558**, A33
- Ballesteros-Paredes, J., Hartmann, L. W., Vázquez-Semadeni, E., Heitsch, F., & Zamora-Avilés, M. A. 2011a, *MNRAS*, **411**, 65
- . 2011b, *MNRAS*, **411**, 65
- Ballesteros-Paredes, J., & Mac Low, M.-M. 2002a, *ApJ*, **570**, 734
- . 2002b, *ApJ*, **570**, 734
- Beaumont, C. N., Offner, S. S. R., Shetty, R., Glover, S. C. O., & Goodman, A. A. 2013, *ApJ*, **777**, 173
- Behnel, S., Bradshaw, R., Citro, C., et al. 2011, *Computing in Science Engineering*, **13**, 31
- Behrendt, M., Burkert, A., & Schartmann, M. 2016, *ApJ*, **819**, L2
- Behroozi, P. S., Wechsler, R. H., & Conroy, C. 2013, *ApJ*, **770**, 57
- Bertoldi, F., & McKee, C. F. 1992, *ApJ*, **395**, 140
- Beuther, H., Schilke, P., Menten, K. M., et al. 2002, *ApJ*, **566**, 945
- Bolatto, A. D., Leroy, A. K., Rosolowsky, E., Walter, F., & Blitz, L. 2008, *ApJ*, **686**, 948
- Bouwens, R. J., Illingworth, G. D., Labbe, I., et al. 2011, *Nature*, **469**, 504
- Bovino, S., Grassi, T., Capelo, P. R., Schleicher, D. R. G., & Banerjee, R. 2016, *A&A*, **590**, A15
- Carniani, S., Maiolino, R., Amorin, R., et al. 2018, *MNRAS*, **478**, 1170
- Ceverino, D., Dekel, A., & Bournaud, F. 2010, *MNRAS*, **404**, 2151
- Clark, P. C., & Bonnell, I. A. 2004, *MNRAS*, **347**, L36
- Clark, P. C., Bonnell, I. A., Zinnecker, H., & Bate, M. R. 2005, *MNRAS*, **359**, 809
- Decataldo et al., in prep. 2019, -, 0, 0
- D’Odorico, V., Feruglio, C., Ferrara, A., et al. 2018, *ApJ*, **863**, L29
- Downes, D., & Solomon, P. M. 1998, *ApJ*, **507**, 615
- Dunlop, J. S., McLure, R. J., Biggs, A. D., et al. 2017, *MNRAS*, **466**, 861
- Elmegreen, B. G., Elmegreen, D. M., Fernandez, M. X., & Lemnios, J. J. 2009, *ApJ*, **692**, 12
- Elmegreen, D. M., Elmegreen, B. G., Ravindranath, S., & Coe, D. A. 2007, *ApJ*, **658**, 763
- Federrath, C., & Klessen, R. S. 2013, *ApJ*, **763**, 51
- Ferlinhoff, C., Brisbin, D., Nikola, T., et al. 2015, *ApJ*, **806**, 260
- Gabor, J. M., & Bournaud, F. 2013, *MNRAS*, **434**, 606
- Gallerani, S., Pallottini, A., Feruglio, C., et al. 2018, *MNRAS*, **473**, 1909
- García-Burillo, S., Combes, F., Hunt, L. K., et al. 2003, *A&A*, **407**, 485
- Genzel, R., Newman, S., Jones, T., et al. 2011, *ApJ*, **733**, 101
- Goldreich, P., & Lynden-Bell, D. 1965, *MNRAS*, **130**, 97
- Goodman, A. A., Alves, J., Beaumont, C. N., et al. 2014, *ApJ*, **797**, 53
- Grassi, T., Bovino, S., Schleicher, D. R. G., et al. 2014, *MNRAS*, **439**, 2386
- Heitsch, F., Ballesteros-Paredes, J., & Hartmann, L. 2009, *ApJ*, **704**, 1735
- Heyer, M., Krawczyk, C., Duval, J., & Jackson, J. M. 2009, *ApJ*, **699**, 1092
- Heyer, M. H., & Brunt, C. M. 2004, *ApJ*, **615**, L45
- Hill, T., Burton, M. G., Minier, V., et al. 2005, *MNRAS*, **363**, 405
- Hodge, J. A., Riechers, D., Decarli, R., et al. 2015, *ApJ*, **798**, L18
- Hodge, J. A., Swinbank, A. M., Simpson, J. M., et al. 2016, *ApJ*, **833**, 103
- Hopkins, P. F., Kocevski, D. D., & Bundy, K. 2014, *MNRAS*, **445**, 823
- Hughes, A., Wong, T., Ott, J., et al. 2010, *MNRAS*, **406**, 2065
- Hughes, A., Meidt, S. E., Colombo, D., et al. 2013, *ApJ*, **779**, 46
- Hunter, J. D. 2007, *Computing in Science Engineering*, 9, 90
- Inoue, S., Dekel, A., Mandelker, N., et al. 2016, *MNRAS*, **456**, 2052
- Jiang, L., Finlator, K., Cohen, S. H., et al. 2016, *ApJ*, **816**, 16
- Jones, E., Oliphant, T., Peterson, P., et al. 2001–, SciPy: Open source scientific tools for Python, [Online; accessed <today>]
- Jones, S. F., Blain, A. W., Assef, R. J., et al. 2017, *MNRAS*, **469**, 4565
- Kassin, S. A., Weiner, B. J., Faber, S. M., et al. 2012, *ApJ*, **758**, 106
- Kauffmann, J., & Pillai, T. 2010, *ApJ*, **723**, L7
- Kauffmann, J., Pillai, T., Shetty, R., Myers, P. C., & Goodman, A. A. 2010, *ApJ*, **716**, 433
- Kauffmann, J., Pillai, T., Zhang, Q., et al. 2017a, *A&A*, **603**, A89
- . 2017b, *A&A*, **603**, A90
- Kennicutt, Jr., R. C. 1989, *ApJ*, **344**, 685
- Kohandel et al., in prep. 2019, -, 0, 0
- Krumholz, M. R., McKee, C. F., & Tumlinson, J. 2009, *ApJ*, **693**, 216
- Labadens, M., Chapon, D., Pomaréde, D., & Teyssier, R. 2012, in *Astronomical Society of the Pacific Conference Series*, Vol. 461, *Astronomical Data Analysis Software and Systems XXI*, ed. P. Ballester, D. Egret, & N. P. F. Lorente, 837
- Larson, R. B. 1981, *MNRAS*, **194**, 809

- Leroy, A. K., Bolatto, A. D., Ostriker, E. C., et al. 2015, *ApJ*, **801**, 25
- Leung, T. K. D., Riechers, D. A., Baker, A. J., et al. 2019, *ApJ*, **871**, 85
- Li, Y., Mac Low, M.-M., & Klessen, R. S. 2005, *ApJ*, **626**, 823
—. 2006, *ApJ*, **639**, 879
- Lombardi, M., Alves, J., & Lada, C. J. 2010, *A&A*, **519**, L7
- Mac Low, M.-M. 1999, *ApJ*, **524**, 169
- Maiolino, R., Carniani, S., Fontana, A., et al. 2015, *MNRAS*, **452**, 54
- Malhotra, S., Kaufman, M. J., Hollenbach, D., et al. 2001, *ApJ*, **561**, 766
- McKee, C. F., & Ostriker, E. C. 2007, *ARA&A*, **45**, 565
- McKee, C. F., & Zweibel, E. G. 1992, *ApJ*, **399**, 551
- Meidt, S. E., Schinnerer, E., García-Burillo, S., et al. 2013, *ApJ*, **779**, 45
- Motte, F., Bontemps, S., Schilke, P., et al. 2007, *A&A*, **476**, 1243
- Mueller, K. E., Shirley, Y. L., Evans, II, N. J., & Jacobson, H. R. 2002, *ApJS*, **143**, 469
- Oka, T., Hasegawa, T., Sato, F., et al. 2001, *ApJ*, **562**, 348
- Ono, Y., Ouchi, M., Curtis-Lake, E., et al. 2013, *ApJ*, **777**, 155
- Pallottini, A., Ferrara, A., Bovino, S., et al. 2017a, *MNRAS*, **471**, 4128
- Pallottini, A., Ferrara, A., Gallerani, S., et al. 2017b, *MNRAS*, **465**, 2540
- Pallottini et al., in prep. 2019, -, 0, 0
- Pan, H.-A., Fujimoto, Y., Tasker, E. J., et al. 2015, *MNRAS*, **453**, 3082
- Planck Collaboration, Ade, P. A. R., Aghanim, N., et al. 2014, *A&A*, **571**, A16
- Rafikov, R. R. 2001, *MNRAS*, **323**, 445
- Romeo, A. B. 1992, *MNRAS*, **256**, 307
- Romeo, A. B., & Wiegert, J. 2011, *MNRAS*, **416**, 1191
- Rosolowsky, E., & Blitz, L. 2005, *ApJ*, **623**, 826
- Rosolowsky, E., & Leroy, A. 2006, *PASP*, **118**, 590
- Rosolowsky, E. W., Pineda, J. E., Kauffmann, J., & Goodman, A. A. 2008, *ApJ*, **679**, 1338
- Rubin, R. H. 1985, *ApJS*, **57**, 349
- Sakamoto, K., Wang, J., Wiedner, M. C., et al. 2008, *ApJ*, **684**, 957
- Sanders, D. B., Scoville, N. Z., & Solomon, P. M. 1985, *ApJ*, **289**, 373
- Scoville, N. Z., & Solomon, P. M. 1974, *ApJ*, **187**, L67
- Shetty, R., Collins, D. C., Kauffmann, J., et al. 2010, *ApJ*, **712**, 1049
- Smit, R., Bouwens, R. J., Carniani, S., et al. 2018, *Nature*, **553**, 178
- Smith, B. D., Turk, M. J., Sigurdsson, S., O’Shea, B. W., & Norman, M. L. 2009, *ApJ*, **691**, 441
- Sparre, M., Hayward, C. C., Springel, V., et al. 2015, *MNRAS*, **447**, 3548
- Swinbank, A. M., Papadopoulos, P. P., Cox, P., et al. 2011, *ApJ*, **742**, 11
- Tan, J. C. 2000, *ApJ*, **536**, 173
- Teyssier, R. 2002, *A&A*, **385**, 337
- Toomre, A. 1964, *ApJ*, **139**, 1217
- Turk, M. J., Smith, B. D., Oishi, J. S., et al. 2011, *ApJS*, **192**, 9
- Vallini, L., Pallottini, A., Ferrara, A., et al. 2018, *MNRAS*, **473**, 271
- van der Walt, S., Colbert, S. C., & Varoquaux, G. 2011, *Computing in Science Engineering*, **13**, 22
- Van Rossum, G., & de Boer, J. 1991, *CWI Quarterly*, **4**, 283
- Wang, B., & Silk, J. 1994, *ApJ*, **427**, 759
- Weingartner, J. C., & Draine, B. T. 2001, *ApJ*, **548**, 296
- Williams, J. P., de Geus, E. J., & Blitz, L. 1994, *ApJ*, **428**, 693
- Wu, B., Tan, J. C., Nakamura, F., Christie, D., & Li, Q. 2018, *PASJ*, **70**, S57